

# Advanced 3D Monte Carlo algorithms for bio-photonic and medical applications

Lewis McMillan



University of  
St Andrews

This thesis is submitted in partial fulfilment for the degree of  
PhD  
at the  
University of St Andrews

March 2019



# Declaration

I, Lewis McMillan, hereby certify that this thesis, which is approximately \*\*\*\*\* words in length, has been written by me, that it is the record of work carried out by me, or principally by myself in collaboration with others as acknowledged, and that it has not been submitted in any previous application for a higher degree.

I was admitted as a research student in September 2015 and as a candidate for the degree of PhD in September 2015; the higher study for which this is a record was carried out in the University of St Andrews between 2015 and 2019.

Date ..... Signature of candidate .....

I hereby certify that the candidate has fulfilled the conditions of the Resolution and Regulations appropriate for the degree of PhD in the University of St Andrews and that the candidate is qualified to submit this thesis in application for that degree.

Date ..... Signature of supervisor .....

Date ..... Signature of supervisor .....



# Abstract

Lorem ipsum dolor sit amet, consectetur adipiscing elit. Ut purus elit, vestibulum ut, placerat ac, adipiscing vitae, felis. Curabitur dictum gravida mauris. Nam arcu libero, nonummy eget, consectetur id, vulputate a, magna. Donec vehicula augue eu neque. Pellentesque habitant morbi tristique senectus et netus et malesuada fames ac turpis egestas. Mauris ut leo. Cras viverra metus rhoncus sem. Nulla et lectus vestibulum urna fringilla ultrices. Phasellus eu tellus sit amet tortor gravida placerat. Integer sapien est, iaculis in, pretium quis, viverra ac, nunc. Praesent eget sem vel leo ultrices bibendum. Aenean faucibus. Morbi dolor nulla, malesuada eu, pulvinar at, mollis ac, nulla. Curabitur auctor semper nulla. Donec varius orci eget risus. Duis nibh mi, congue eu, accumsan eleifend, sagittis quis, diam. Duis eget orci sit amet orci dignissim rutrum.

Nam dui ligula, fringilla a, euismod sodales, sollicitudin vel, wisi. Morbi auctor lorem non justo. Nam lacus libero, pretium at, lobortis vitae, ultricies et, tellus. Donec aliquet, tortor sed accumsan bibendum, erat ligula aliquet magna, vitae ornare odio metus a mi. Morbi ac orci et nisl hendrerit mollis. Suspendisse ut massa. Cras nec ante. Pellentesque a nulla. Cum sociis natoque penatibus et magnis dis parturient montes, nascetur ridiculus mus. Aliquam tincidunt urna. Nulla ullamcorper vestibulum turpis. Pellentesque cursus luctus mauris.



# Contents

<b>1 Computational modelling of tissue ablation</b>	<b>1</b>
1.1 Introduction and background . . . . .	1
1.2 Methods . . . . .	2
1.2.1 Monte Carlo radiation transport (MCRT) . . . . .	2
1.2.2 Heat transport . . . . .	4
1.2.3 Tissue Damage . . . . .	10
1.3 <i>In silca</i> results . . . . .	11
1.3.1 Results . . . . .	12
1.4 Conclusion . . . . .	13



# Chapter 1

## Computational modelling of tissue ablation

### 1.1 Introduction and background

Lasers are used in wide variety of medical procedures not limited to: coagulating scalpels, port wine stain removal, tattoo removal, hair removal, and skin rejuvenation [1–5]. One class of laser used in these procedures are ablative lasers. Ablative lasers are usually high powered lasers targeted at a specific chromophore in the skin, to partially or fully remove layers of skin. These types of lasers are commonly used for aesthetic procedures such as: skin rejuvenation [5], and removal of various diseases such as Rhinophyma [6] or lesions/nodules [7]. They have also recently been investigated as a means of better drug delivery in the skin for photo-dynamic therapy (PDT) treatments [8].

One downside to using lasers to remove tissue, it that unlike a scalpel, where the surgeon has full control of the depth of the incision, ablative lasers are not as predictable. Lasers can also cause unwanted thermal damage to the surrounding areas, leading to unwanted effects. Ablative lasers, and fractionated ablative lasers (ablative lasers where the power is spread over several beams, such as to leave viable tissue around zones of damaged/necrotic tissue [9]). Currently the only reliable method to measure the depth of the ablative holes, is via a biopsy, which is an invasive procedure. We propose to use optical coherence tomography (OCT) to measure the ablative crater non-invasively *in-vivo*. The OCT measurements are then backed up by a computational model. This computational model could then be used to predict the depth of the ablative crater when using a certain power for various different applications such as: laser assisted drug delivery, and various cosmetic applications.

This chapter examines using Monte Carlo radiation transport techniques coupled to a heat transfer simulation, in order to study the thermal damage to tissue due to fractional lasers. We present experimental work carried out by our collaborators at the University of Dundee and the photobiology department at Ninewells hospital. This experimental work was carried out on porcine tissue, using CO<sub>2</sub> and Er:YAG lasers.

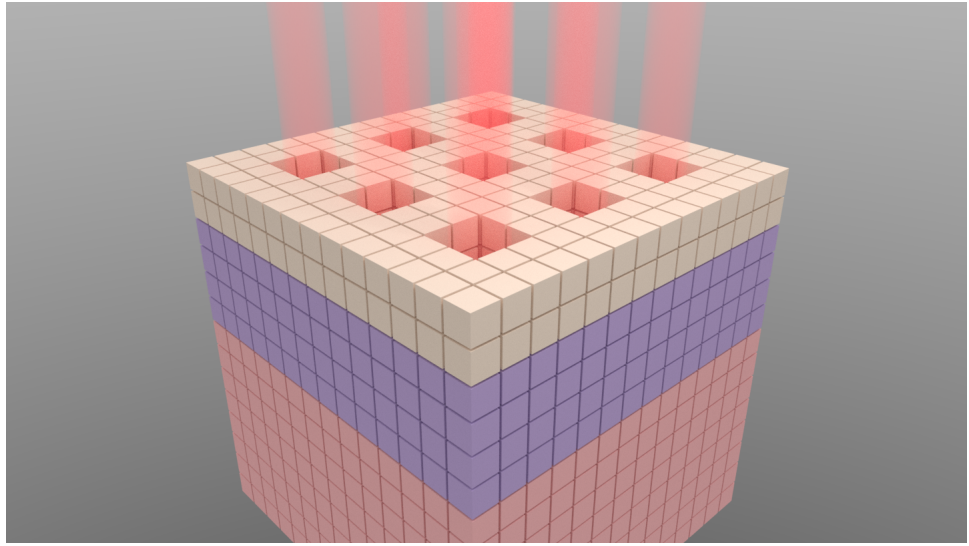


**Figure 1.1:** Example of a possible voxel model, with three different layers, various holes due to ablative pixel beam lasers. Each voxel represents a different optical/thermal property of the tissue medium.

## 1.2 Methods

In order to replicate the experimental work *in silica*, our numerical model has three main portions. The first is the Monte Carlo radiation transport method (MCRT) that models light transport through tissue so that we can calculate the laser energy deposited as a function of time and space. The second, a finite difference method (FDM) which is used to calculate the heat diffusion within the tissue due to the absorbed laser energy. Finally, a tissue damage model to track the damage to the tissue caused by the laser. All these individual portions are connected together to create our numerical model. Each portion of the numerical model is described below in more detail.

### 1.2.1 Monte Carlo radiation transport (MCRT)

MCRT is the ‘gold standard’ for simulating the transport of light through biological tissue \*ref\*. It uses interaction probabilities and random numbers in order to model the ‘random walk’ that photons undergo in a turbid medium. These ‘packets’ can undergo go scattering, absorption and various other physical process [10, 11]. MCRT has been used to model light-tissue interactions in many different medical and biophotonic applications [12]\*more refs\*. MCRT is used here to calculate the energy deposited by the laser, which is then passed to the heat transport simulation.

The tissue medium for the MCRT and heat transport simulations is a 3D voxel model (Fig. 1.1). This allows the variation of optical and thermal properties from voxel to voxel, making it the ideal type of grid for modelling tissue ablation. We use  $n \times n \times n$  voxels \*still changing this\*, representing a tissue sample size of  $1.1 \times 1.1 \times 0.5$  cm. We assume the porcine skin is uniform, so that initially our voxel model is uniform, and the optical properties of porcine skin at the wavelength of interest is that of water, see Fig. 1.9.

The original MCRT code was developed for astronomy applications [13, 14], and has since

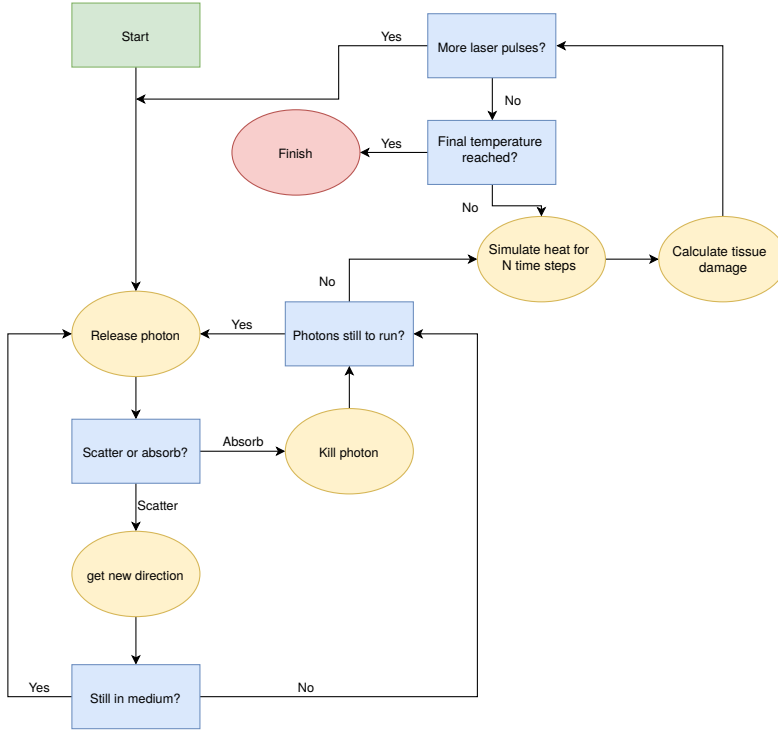


**Figure 1.2:** Flowchart of the tissue ablation algorithm.

been adapted for medical applications [12, 15].

Figure 1.2. shows the overall algorithm for the simulation, including the MCRT portion. The MCRT portion of the algorithm begins with determining where the photon enters the medium. This is calculated by randomly selecting one of the pixel beams, from the 9x9 array of pixel beams. Next the position on the surface of the medium is calculated. As the profile of the pixel beams are unknown, they are assumed to be uniformly circular \*maybe change to gaussian??\*. Thus, the packets position is uniformly sampled on a circle the width of the pixel beam.

Once the packet enters the simulation, a propagation distance for the packets is calculated using Eq. (1.1). The packet then moves this distance before undergoing an interaction event. This can be either scattering or absorption. This process is repeated until the photon has either been absorbed or exits the medium.

$$L = -\frac{\ln(\xi)}{\mu_a} \quad (1.1)$$

Where:

$\xi$  a random number ( $\tau = -\ln(\xi)$ ,  $\tau$  is the optical depth);

$\mu_a$  is the absorption coefficient;

L is the physical distance.

The above process is repeated until all the photons have been absorbed or have escaped the tissue medium. We use 5 million photons per MCRT simulation run.

We calculate the absorbed energy using the path length counter method devised by Lucy [16]. The energy absorbed per voxel is calculated as:

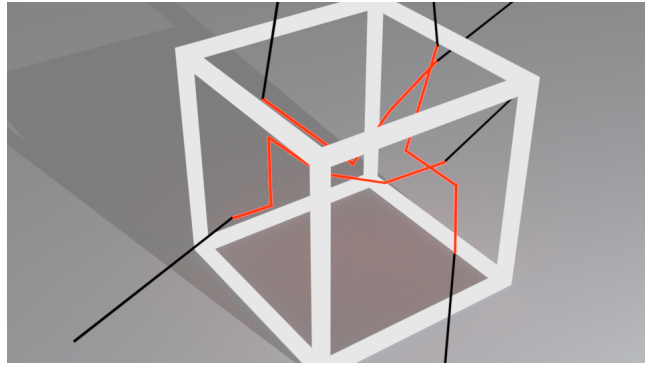


**Figure 1.3:** Red lines are photon paths within a voxel. Black lines photon paths outwith the voxel. Red photon paths are summed up in order to calculate the absorbed energy within each voxel.

$$E_i^{abs} = \frac{L}{N\Delta V_i} \sum \mu_a s \quad (1.2)$$

Where:

$L$  is luminosity [W];

$N$  is the number of photons;

$\Delta V_i$  is the volume of the  $i^{th}$  voxel [ $m^{-3}$ ];

$\mu_{a,i}$  is the absorption coefficient of the  $i^{th}$  voxel [ $cm^{-1}$ ];

and  $s$  is the pathlength of a photon packet through the  $i^{th}$  voxel [cm].

This grid of absorbed energy is then passed to the heat transport portion of the simulation.

### 1.2.2 Heat transport

In order to model the transport of heat in porcine skin, we use the standard parabolic heat equation:

$$\rho c_p \frac{\partial T}{\partial t} = \nabla \cdot (\kappa \nabla T) + \dot{q} \quad (1.3)$$

Where:

$T(x, y, z, t)$  is the temperature as a function of time and space [K];

$\kappa$  is the thermal conductivity [ $Wm^{-1}K^{-1}$ ];

$\rho$  is the density [ $Kgm^{-3}$ ];

$c_p$  the specific heat capacity [ $JK^{-1}$ ];

$\dot{q}(x, y, z, t)$  is the source/sink term as a function of time and space [ $Wm^{-3}$ ].

We assume that  $\kappa$  is constant during heat transport and only changes between heat transport and MCRT portions of the simulation (see Section Tissue damage), thus:

$$\frac{\partial T}{\partial t} = \alpha \nabla^2 T + \dot{q} \quad (1.4)$$

Where  $\alpha = \frac{\kappa}{\rho c_p}$  is the thermal diffusivity [ $m^2 s^{-1}$ ]

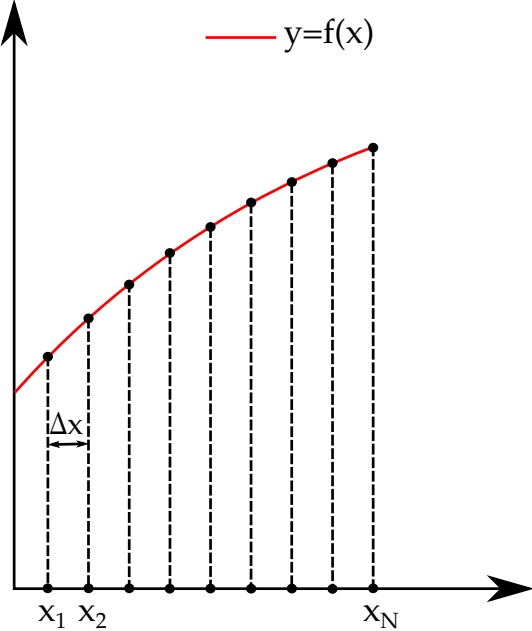


**Figure 1.4:** Finite difference methods discretisation of  $f(x)$ .

The  $\dot{q}$  term is a heat source/sink term. The heat source in this simulation is due to the laser, and we assume the only loss of heat to the surrounding medium is via convection and conduction.

These boundary conditions must be considered. All faces of the cube, bar the laser facing face, are considered to be pinned at  $5^{\circ}\text{C}$ , as the porcine skin was kept cooled prior to experimental work. The laser facing face has a simple convective BC:

$$\dot{q}_c = -hA(T - T_{\infty}) \quad (1.5)$$

Where:

$h$  is the heat transfer coefficient [ $\text{W m}^{-2} \text{K}$ ];

and  $A$  is the area of the grid element, that is radiating/convicting heat away [ $\text{m}^{-2}$ ].

As Eq. (1.4) is generally hard to solve in arbitrary geometries with complex boundary conditions we employ a numerical method to solve Eq. (1.4). The numerical method we employ in order to solve Eq. (1.3) is a the finite difference method (FDM) [17]. FDM is derived from the Taylor series approximation for derivatives. A function  $f(x)$  is discretised onto a grid with  $N$  nodes (see Fig. 1.4). Then at node  $i$  we can use the Taylor series approximation in the forward (+ive  $x$  direction) and backward (-ive  $x$  direction), and combine the 1<sup>st</sup> and 2<sup>nd</sup> derivatives in 1D, where:  $i$  is the grid point at  $x_o$ ,  $i+1$  is the point at  $x_0 + \Delta x$ , and  $i-1$  is the grid point at  $x_0 - \Delta x$ .

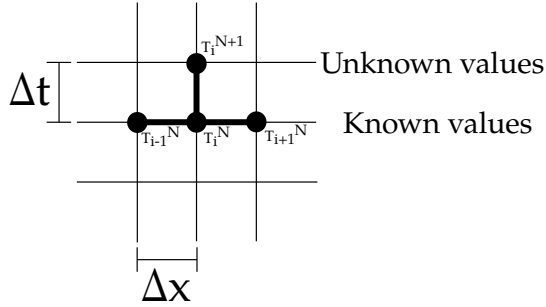


**Figure 1.5:** Finite difference method stencil for simple explicit scheme

$$\frac{df}{dx} = \frac{f_{i+1} - f_i}{\Delta x} \quad (\text{forward}) \quad (1.6a)$$

$$\frac{df}{dx} = \frac{f_i - f_{i-1}}{\Delta x} \quad (\text{backward}) \quad (1.6b)$$

$$\frac{df}{dx} = \frac{f_{i+1} - f_{i-1}}{2\Delta x} \quad (\text{central}) \quad (1.6c)$$

$$\frac{d^2f}{dx^2} = \frac{f_{i-1} - 2f_i + f_{i+1}}{\Delta x^2} \quad (\text{central}) \quad (1.6d)$$

Thus Eq. (1.4), in 1D, becomes:

$$T_{i+1}^{n+1} = \Delta t \alpha \frac{T_{i-1}^n - 2T_i^n + T_{i+1}^n}{\Delta x^2} + T_i^n + \dot{q} \quad (1.7)$$

Equation (1.7) is called the ‘simple explicit form of finite-difference approximation’ [17]. Figure 1.5 shows the ‘stencil’ of this scheme, where there are three known points at time  $N$ , and just one unknown at time  $N+1$ . We use a simple explicit scheme here, due to its ease of implementation. This yields for the more general 3D case:

$$\begin{aligned} U_{xx} &= \frac{\alpha}{\Delta x^2} (T_{i-1,j,k}^N - 2T_{i,j,k}^N + T_{i+1,j,k}^N) \\ U_{yy} &= \frac{\alpha}{\Delta y^2} (T_{i,j-1,k}^N - 2T_{i,j,k}^N + T_{i,j+1,k}^N) \\ U_{zz} &= \frac{\alpha}{\Delta z^2} (T_{i,j,k-1}^N - 2T_{i,j,k}^N + T_{i,j,k+1}^N) \\ T_{i,j,k}^{N+1} &= \Delta t (U_{xx} + U_{yy} + U_{zz}) + T_{i,j,k}^N + \frac{\alpha \Delta t}{\kappa} q_L \end{aligned}$$

Where:

$T_{i,j,k}^{N+1}$  is the new temperature at node  $i, j, k$  [K];

$T_{i,j,k}^N$  is the temperature at node  $i, j, k$  at the current time step [K];

$\alpha$  is the thermal diffusivity [ $m^2 s^{-1}$ ];

$\kappa$  is the thermal conductivity [ $W/m \cdot K$ ];

$\Delta x$  etc. is the size of the grid element in the  $p^{th}$  direction [m].

Incorporating B.Cs on the top air exposed face:

$$U_{zz} = \frac{\alpha}{\Delta z^2} \left( \frac{2\Delta z}{\kappa} (-h(T_{i,j,k}^N - T_\infty^N)) - 2T_{i,j,k}^N + 2T_{i,j,k+1}^N \right) \quad (1.8)$$

As we are using a simple explicit FDM, the time step is constrained in order to make the solution stable. For a cubic 3D FDM without prescribed flux BCs, yields the constraint:  $\Delta t \leq \frac{\alpha \Delta x^2}{2\beta}$ . However as we have a flux prescribed boundary condition, the constraint on the time is more severe. Along with this time restraint, the pulse length of the laser also has to be considered. If the time step of the heat simulation is too large it will not account for the heat deposited by the laser. Thus, the timestep has to be an order of magnitude smaller than the shortest laser pulse.

As the timestep is small, and the grid resolution large, the resultant simulation is slow. Thus the code has been fully parallelised to improve performance. Both the MCRT and heat simulation are independently parallelised. As MCRT is classed as an ‘embarrassingly parallel’ problem, this portion of the simulation is run on N cores and the results collated and passed to the heat simulation. The heat simulation is parallelised using a technique called ‘halo swapping’. This involves splitting up the computational domain, in this case the tissue medium, and separate calculations run on each separate core. They then pass the information from the edge of each of their respective domains to their neighbours (see Fig. 1.7).

After the heat transport has been completed, the grid of temperatures is passed to the tissue damage portion of the simulation.

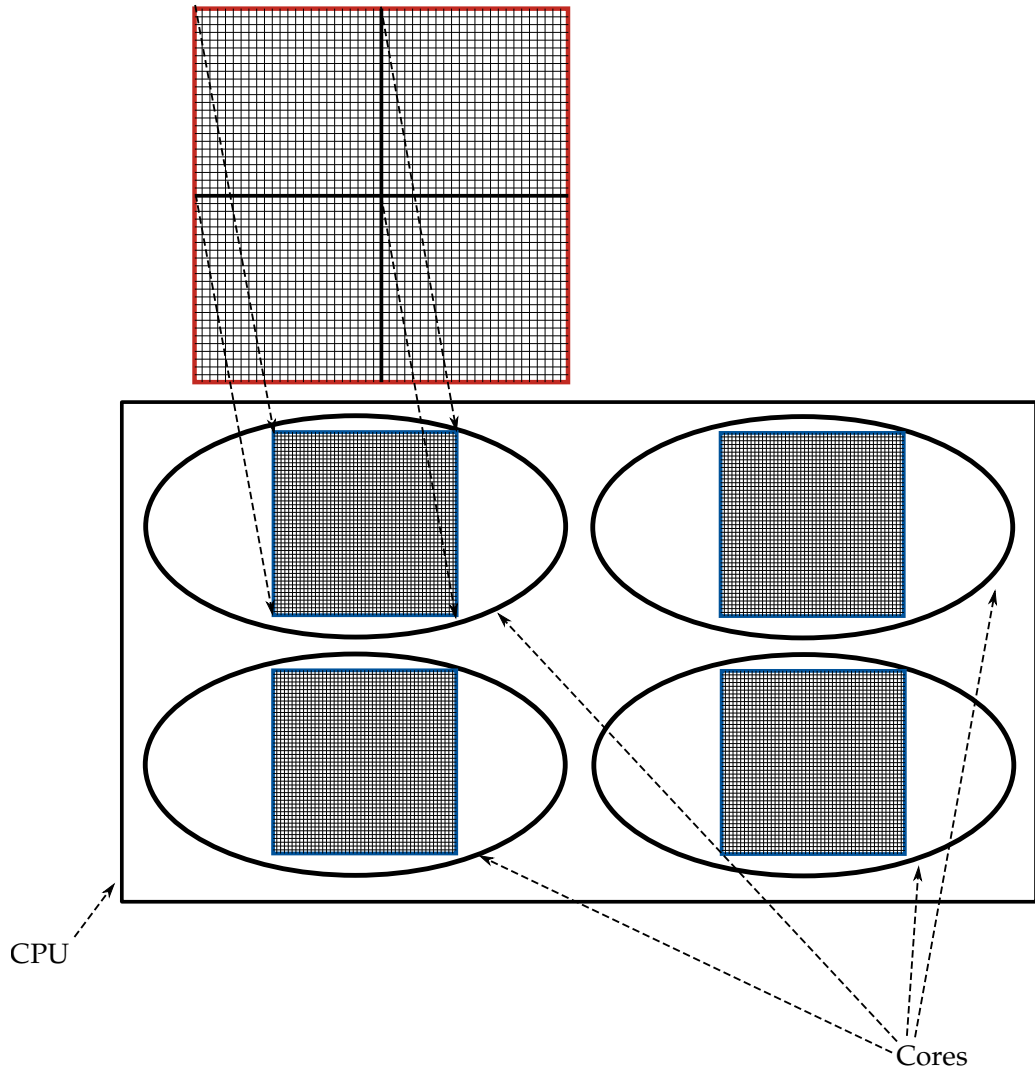


**Figure 1.6:** Computational domain decomposition. Total computational domain is evenly divided between cores in the CPU. This is done via layers of the domain in the  $z$  direction. Information is passed to/from cores via the ‘halo swap’ process (see Fig. 1.7).

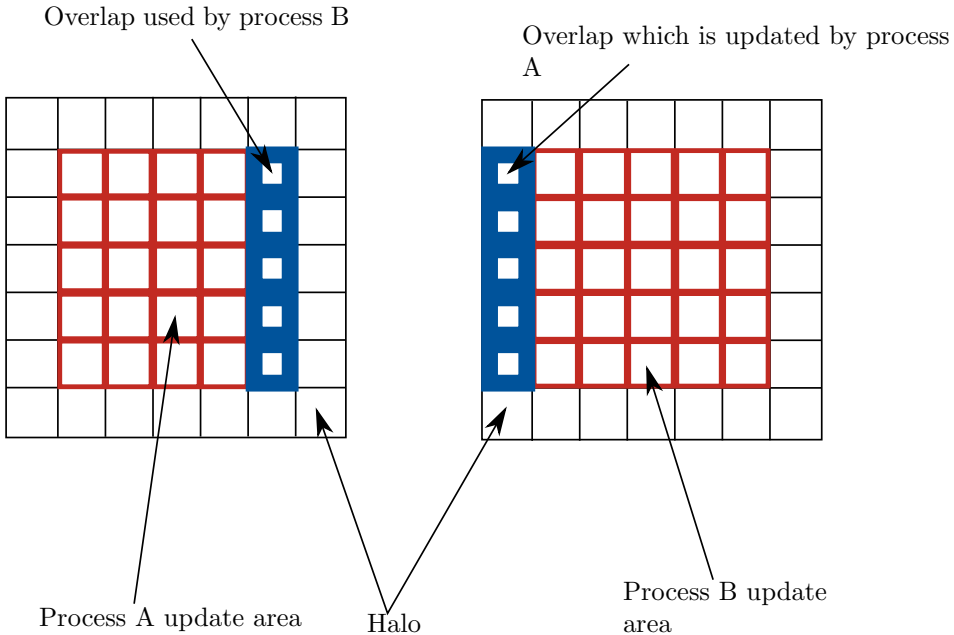


**Figure 1.7:** Halo swapping. Process A updates the area in red and blue on the left. It updates the blue area which is sent to process B as B's 'halo'. Process B cannot update its own halo, but rather updates the halo for process A.

#### Validation of heat transport numerical method

In order to validate the numerical method we employ to solve the heat equation, we compare the numerical method against an easily solvable case. Assuming a separable solution in Cartesian for the heat equation yields:

$$\begin{aligned} T(x, y, z, t) = & (A_1 \cos(\alpha x) + A_1 \sin(\alpha x)) \\ & (B_1 \cos(\beta y) + B_1 \sin(\beta y)) \\ & (C_1 \cos(\gamma z) + C_1 \sin(\gamma z)) e^{-\kappa \mu^2 t} \\ \mu^2 = & \alpha^2 + \beta^2 + \gamma^2 \end{aligned}$$

Then for a cube, side  $L$ , at  $t = 0$  the temperature everywhere in the cube is  $37^\circ\text{C}$ . The boundary conditions are:

$$\begin{aligned} T(0, y, z, t) = T(x, 0, z, t) = T(x, y, 0, t) &= 0^\circ\text{C} \\ T(L, y, z, t) = T(x, L, z, t) = T(x, y, L, t) &= 0^\circ\text{C} \end{aligned}$$

$$\therefore A_1 = B_1 = C_1 = 0 \text{ and } \alpha = \frac{\pi n}{L}, \beta = \frac{\pi m}{L}, \gamma = \frac{\pi p}{L} \quad (1.9)$$

$$T_{nmp}(x, y, z, t) = A_{nmp} \sin\left(\frac{\pi n x}{L}\right) \cdot \sin\left(\frac{\pi m y}{L}\right) \cdot \sin\left(\frac{\pi p z}{L}\right) \quad (1.10)$$

This yields the following solution for the heat equation using the principle of superposition and the boundary conditions:

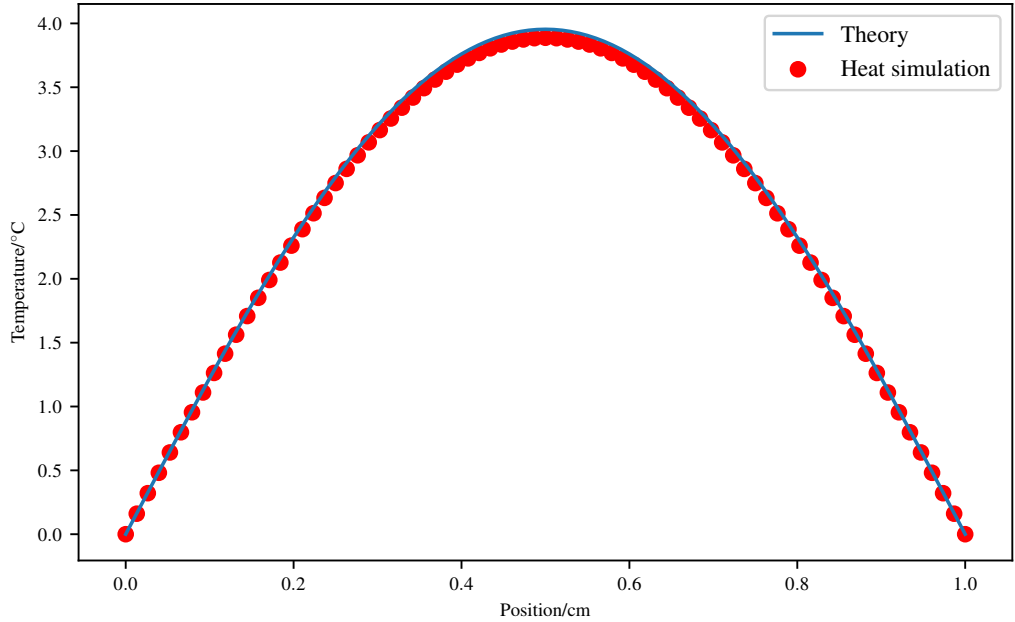


**Figure 1.8:** Comparison between analytical solution and numerical method.

$$T(x, y, z, t) = \sum_{n=1,3,\dots}^{\infty} \sum_{m=1,3,\dots}^{\infty} \sum_{p=1,3,\dots}^{\infty} \frac{2368}{\pi^3 nmp} \sin\left(\frac{\pi nx}{L}\right) \sin\left(\frac{\pi my}{L}\right) \sin\left(\frac{\pi pz}{L}\right) e^{(-\lambda^2 t)} \quad (1.11)$$

Where:

$$\lambda^2 = \kappa\pi^2\left(\frac{n^2}{L^2} + \frac{m^2}{L^2} + \frac{p^2}{L^2}\right);$$

$n, m, p$  are odd integers;

and  $L$  is the length of the cube.

At time,  $t = 0.1$ s, a slice through the middle of the medium yields Fig. 1.8.

### 1.2.3 Tissue Damage

The final portion of the simulation is the tissue damage model. We use the Arrhenius damage model, originally used as a kinetic model of reaction products in chemistry [18]. It has since been adapted by various authors for modelling tissue damage [19, 20].

$$\Omega(t) = \int_{t_i}^{t_f} Ae^{-\frac{\Delta E}{RT}} d\tau \quad (1.12)$$

Where:

$\Omega$  is the damage value;

$A$  is ‘frequency factor’ [ $s^{-1}$ ];

$\Delta E$  is activation energy [ $J/mol$ ];

$R$  is the universal gas constant [ $Jmol^{-1}K^{-1}$ ];

$T$  is the temperature [ $K$ ];

and  $t_i$  and  $t_f$  are the initial time and final time at  $t_{crit}$ .

It is reported that a value of  $\Omega$  of 0.53, 1.0, and  $10^4$  relate to first, second, and third degree burns respectively [21]. We use the Arrhenius damage model in order to better understand the amount of damage caused by the laser in the non-ablated areas of tissue. This can give us an insight into the various physical phenomena encountered in the OCT results.

We model tissue damage in four main sections: coagulated, dehydrated, carbonized, and finally ablated sections.

Coagulated tissue is the the areas of the tissue where the temperature is above  $43^\circ\text{C}$ , the threshold for damage. When areas of the tissue reach  $100^\circ\text{C}$  water begins to boil. This acts as a large heat sink for the absorbed laser energy, and is modeled as;

$$Q_{vaporisation} = M_{voxel} L_{vaporisation} \quad (1.13)$$

Where:

$Q_{vaporisation}$  is energy in Joules required to boil off the water in a voxel [ $J$ ];

$M_{voxel}$  is the mass of a voxel [ $\text{Kg}$ ];

and  $L_{vaporisation}$  is the latent heat of vaporization for water [ $\text{JK}^{-1}$ ].

As water boils off, the water content of each voxel changes. This affects the absorption coefficient, density, thermal conductivity, and heat capacity. Each of these vary linearly with water content per voxel;

$$W = W_{init} - \left( W_{init} * \left( \frac{Q_{current}}{Q_{vaporisation}} \right) \right) \quad (1.14)$$

$$\rho = 6.16 \cdot 10^{-5} W + 9.38 \cdot 10^{-4} \quad (1.15)$$

$$c = 2.5 \cdot 10^3 W + 1.7 \cdot 10^3 \quad (1.16)$$

$$\kappa = \rho \cdot 10^{-3} (0.454 W + 0.174) \quad (1.17)$$

Where:

$W$  is the water content (i.e  $W = 0.7$  equates to 70% water content);

$W_{init}$  is the initial water content;

$Q_{current}$  is the total energy absorbed by the  $i^{th}$  voxel since the temperature reached  $100^\circ\text{C}$ ;

$\kappa$  is the Thermal conductivity [ $\text{Wm}^{-1}\text{K}^{-1}$ ];

and  $c$  is the heat capacity [ $\text{JKg}^{-1}\text{K}^{-1}$ ].

We define the ablation temperature ( $T_a$ ) as occurring between  $173$  and  $450^\circ\text{C}$  [22]. At the  $T_a$  the tissue is removed and set the thermal and density properties to that of air.

The tissue structure is then fed back to the MCRT model and the whole process repeats until the average temperature of the model is under  $43^\circ\text{C}$ . This process is outlined in Fig. 1.2.

### 1.3 In silca results

#### Optical & thermal properties

As both of the lasers used in the experimental work are infrared lasers, this means that the optical properties are dominated by water absorption (see Fig. 1.9). Er:YAG has a wavelength

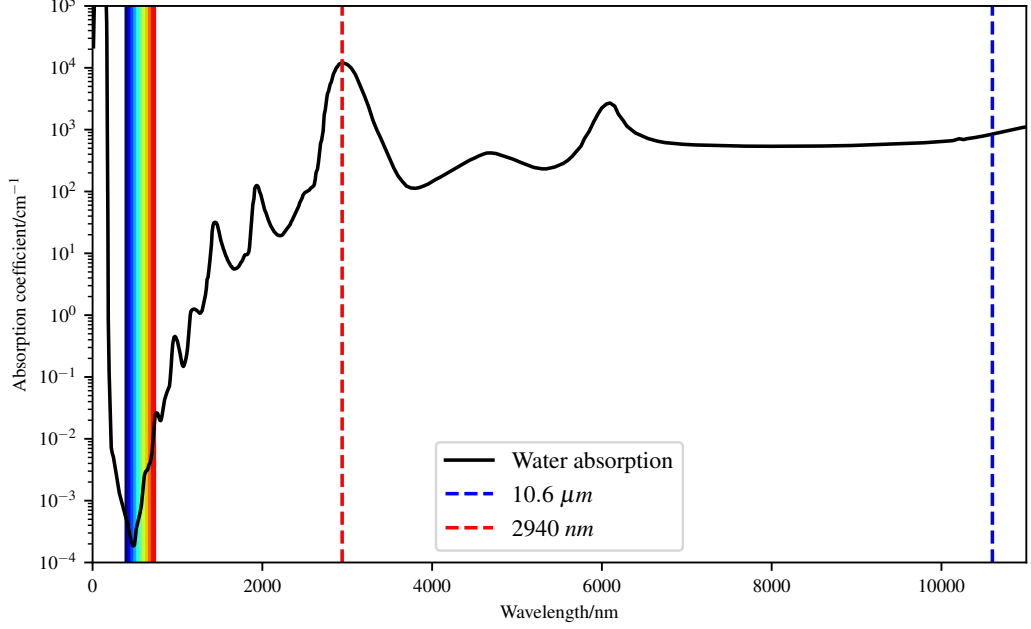


**Figure 1.9:** Water absorption coefficient for wavelengths 0-12000nm [23]. Data shows that water is highly absorbing at large wavelengths.

•	Thermal conductivity, $\kappa$	Density, $\rho$	Heat capacity, $c$
Tissue	$\rho \cdot 10^{-3}(0.454 W + 0.174)$	$6.16 \cdot 10^{-5} W + 9.38 \cdot 10^{-4}$	$2.5 \cdot 10^3 W + 1.7 \cdot 10^3$
Air	$ae^{-b(T-273.15)} + c$	$\frac{p_{atm}}{R_{spec}T}$	1006

**Table 1.1:** blah blah

2940 nm which corresponds to an absorption coefficient of water:  $\sim 11200 \text{ cm}^{-1}$ . The CO<sub>2</sub> laser has a wavelength 10.6  $\mu\text{m}$  which corresponds to an absorption coefficient of  $\sim 850 \text{ cm}^{-1}$ . As the absorption coefficient is large, we assume that scattering is negligible at these wavelength. Table 1.1 summarises the thermal properties for tissue and air used in the simulations.

### 1.3.1 Results

We model the porcine skin as a cuboid dimensions:  $1.1 \times 1.1 \times 0.5 \text{ cm}$ . The initial temperature of the porcine skin is assumed to be around 5°, as the tissue was kept on ice. As mentioned in the previous sections, there are several unknowns in the model:  $T_a$ , water content, temperature of air after ablation. Therefore we run several models so that the full parameter space of these unknowns can be explored.

#### Investigating ablation temperature, $T_a$

Various literature sources report the ablation temperature ranging from 173° to 450°\*cite this\*. Thus, we run several models over this range. Fig. 1.10 shows how  $T_a$  affects the crater depth as a function of pixel beam energy. At lower pixel beam energies, the tissue ablation temperature has little to no effect on the crater depth. At higher energies,  $\geq 125 \text{ mJ}$ , the value of  $T_a$  ha

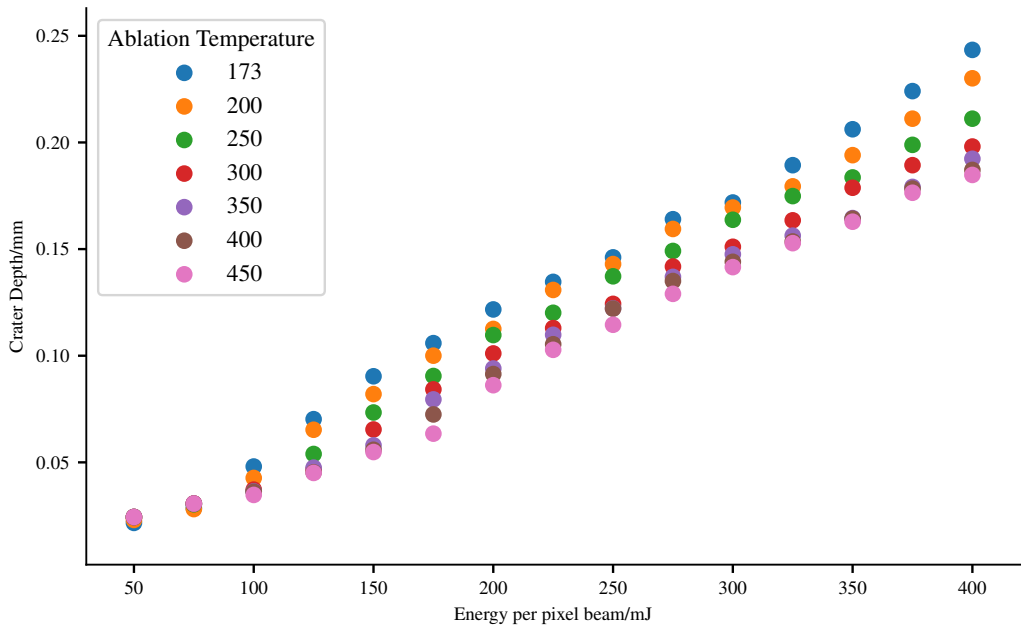


**Figure 1.10:** Simulation of  $CO_2$  ablative laser crater depths as a function of pixel beam energy for various  $T_a$ s.

a larger effect. For example at  $400\text{ mJ}$  there is a difference in the crater depth of  $\sim 0.05\text{ mm}$  between the lowest and highest  $T_a$ .

#### Investigating water content

#### Investigating temperature of air after ablation

## 1.4 Conclusion



# Bibliography

- [1] Saeid Amini-Nik, Darren Kraemer, Michael L Cowan, Keith Gunaratne, Puvindran Nadesan, Benjamin A Alman, and RJ Dwayne Miller. Ultrafast mid-ir laser scalpel: protein signals of the fundamental limits to minimally invasive surgery. *PLoS One*, 5(9):e13053, 2010.
- [2] Oon Tian Tan, Karen Sherwood, and Barbara A Gilchrest. Treatment of children with port-wine stains using the flashlamp-pulsed tunable dye laser. *New England journal of medicine*, 320(7):416–421, 1989.
- [3] Marina Kuperman-Beade, Vicki J Levine, and Robin Ashinoff. Laser removal of tattoos. *American journal of clinical dermatology*, 2(1):21–25, 2001.
- [4] Se Hwang Liew. Laser hair removal. *American journal of clinical dermatology*, 3(2):107–115, 2002.
- [5] Christina A Hardaway and E Victor Ross. Nonablative laser skin remodeling. *Dermatologic clinics*, 20(1):97–111, 2002.
- [6] Stanley M Shapshay, M Stuart Strong, Gaspar W Anastasi, and Charles W Vaughan. Removal of rhinophyma with the carbon dioxide laser: a preliminary report. *Archives of Otolaryngology*, 106(5):257–259, 1980.
- [7] Roberto Valcavi, Fabrizio Riganti, Angelo Bertani, Debora Formisano, and Claudio M Pacella. Percutaneous laser ablation of cold benign thyroid nodules: a 3-year follow-up study in 122 patients. *Thyroid*, 20(11):1253–1261, 2010.
- [8] Merete Haedersdal, Fernanda H Sakamoto, William A Farinelli, Apostolos G Doukas, Josh Tam, and R Rox Anderson. Fractional co<sub>2</sub> laser-assisted drug delivery. *Lasers in Surgery and Medicine: The Official Journal of the American Society for Laser Medicine and Surgery*, 42(2):113–122, 2010.
- [9] Dieter Manstein, G Scott Herron, R Kehl Sink, Heather Tanner, and R Rox Anderson. Fractional photothermolysis: a new concept for cutaneous remodeling using microscopic patterns of thermal injury. *Lasers in Surgery and Medicine: The Official Journal of the American Society for Laser Medicine and Surgery*, 34(5):426–438, 2004.
- [10] Gang Yao and Lihong V Wang. Monte carlo simulation of an optical coherence tomography signal in homogeneous turbid media. *Physics in Medicine & Biology*, 44(9):2307, 1999.
- [11] AJ Welch, Craig Gardner, Rebecca Richards-Kortum, Eric Chan, Glen Criswell, Josh Pfefer, and Steve Warren. Propagation of fluorescent light. *Lasers in Surgery and Medicine: The Official Journal of the American Society for Laser Medicine and Surgery*, 21(2):166–178, 1997.

- [12] Catherine Louise Campbell, Kenny Wood, RM Valentine, C Tom A Brown, and H Moseley. Monte carlo modelling of daylight activated photodynamic therapy. *Physics in Medicine & Biology*, 60(10):4059, 2015.
- [13] Kenneth Wood and RJ Reynolds. A model for the scattered light contribution and polarization of the diffuse  $\text{H}\alpha$  galactic background. *The Astrophysical Journal*, 525(2):799, 1999.
- [14] Kenneth Wood, LM Haffner, RJ Reynolds, John S Mathis, and Greg Madsen. Estimating the porosity of the interstellar medium from three-dimensional photoionization modeling of  $\text{H}\text{II}$  regions. *The Astrophysical Journal*, 633(1):295, 2005.
- [15] Isla Rose Mary Barnard, Patrick Tierney, Catherine Louise Campbell, Lewis McMillan, Harry Moseley, Ewan Eadie, Christian Tom Alcuin Brown, and Kenneth Wood. Quantifying direct dna damage in the basal layer of skin exposed to uv radiation from sunbeds. *Photochemistry and photobiology*.
- [16] LB Lucy. Computing radiative equilibria with monte carlo techniques. *Astronomy and Astrophysics*, 344:282–288, 1999.
- [17] Necati Ozisik. *Finite difference methods in heat transfer*. CRC press, 1994.
- [18] John A Pearce. Relationship between arrhenius models of thermal damage and the cem 43 thermal dose. In *Energy-based Treatment of Tissue and Assessment V*, volume 7181, page 718104. International Society for Optics and Photonics, 2009.
- [19] FC Jr Hendriques. Studies of thermal injury; the predictability and the significance of thermally induced rate processes leading to irreversible epidermal injury. *Arch. Pathol. (Chic)*, 43:489–502, 1947.
- [20] SC Jiang, N Ma, HJ Li, and XX Zhang. Effects of thermal properties and geometrical dimensions on skin burn injuries. *Burns*, 28(8):713–717, 2002.
- [21] KR Diller and LJ Hayes. A finite element model of burn injury in blood-perfused skin. *Journal of biomechanical engineering*, 105(3):300–307, 1983.
- [22] Miron Gerstmann, Y Linenberg, Abraham Katzir, and Solange Akselrod. Char formation in tissue irradiated with a co 2 laser: model and simulations. *Optical Engineering*, 33(7):2343–2352, 1994.
- [23] David J Segelstein. *The complex refractive index of water*. PhD thesis, University of Missouri–Kansas City, 1981.